Comptes Rendus
Géoscience — Sciences de la Planète
Supplementary material to the article available at:
https://doi.org/10.5802/crgeos.84

Supplementary material: Experimental determination of H_2O and CO_2 solubilities of mafic alkaline magmas from Canary Islands

María Jiménez-Mejías *, [a, b, c, d], **Joan Andújar** [a], **Bruno Scaillet** [a] **and Ramón Casillas** [d]

[a] Institut des Sciences de la Terre d'Orléans (ISTO), UMR 7327, Université d'Orléans, CNRS, BRGM, 1A rue de la Férollerie, F-45071 Orléans, France

[b] Geosciences Barcelona (GEO3BCN-CSIC), C/Lluis Solé i Sabarís s/n, 08028, Barcelona, Spain

[c] Instituto Geográfico Nacional, Centro Geofísico de Canarias, C/ La Marina 20, 2°, 38001 Santa Cruz de Tenerife, Spain

[d] Departamento de Biología Animal, Edafología y Geología. Facultad de Ciencias. Universidad de La Laguna. C/Astrofísico Francisco Sánchez S/N. 38206. La Laguna, Santa Cruz de Tenerife, Spain

E-mails: maria.jimenez@cnrs-orleans.fr (M. Jiménez-Mejías), juan.andujar@cnrs-orleans.fr (J. Andújar), bruno.scaillet@cnrs-orleans.fr (B. Scaillet), rcasilla@ull.es (R. Casillas)

1. Experimental and analytical methods

1.1. *Starting material*

Experiments were performed on two natural compositions from historical eruptions of Tenerife (Canary Islands, Spain): a basanite scoria from the northeastern vent of Fasnia volcano [1705 A.D; Albert et al., 2015] and a phonotephrite from the scoria cone of Garachico volcano [1706 A.D.; Carracedo and Perez-Torrado, 2013; Solana, 2012] (Figure 1).

The natural samples were prepared by crushing and milling scoria fragments, which were finely ground under ethanol using an agate mortar. In order to obtain homogeneous and nominally anhydrous glasses, the resulting powder was held in a Pt crucible for a two-step fusion (with grounding in between) at 1400 °C during 4 h in open-air atmosphere and rapidly quenched in a water container at room temperature. The composition of the starting materials was analysed by electron microprobe (EPMA, Table 1) to ensure that no significant compositional variation (i.e., Na or Fe loss toward the crucible) occurred during the melting process. The resulting glass compositions tightly agree (within errors) with X-ray fluorescence analysis performed independently on the samples (Table 1).

Although Garachico rock lies on the basanite-phonotephrite boundary (Figure 1b) in the total alkalis versus silica classification [TAS, Le Bas et al., 1986], its mineral assemblage corresponds to that of a phonotephrite from Tenerife [Ablay et al., 1998],

* Corresponding author.

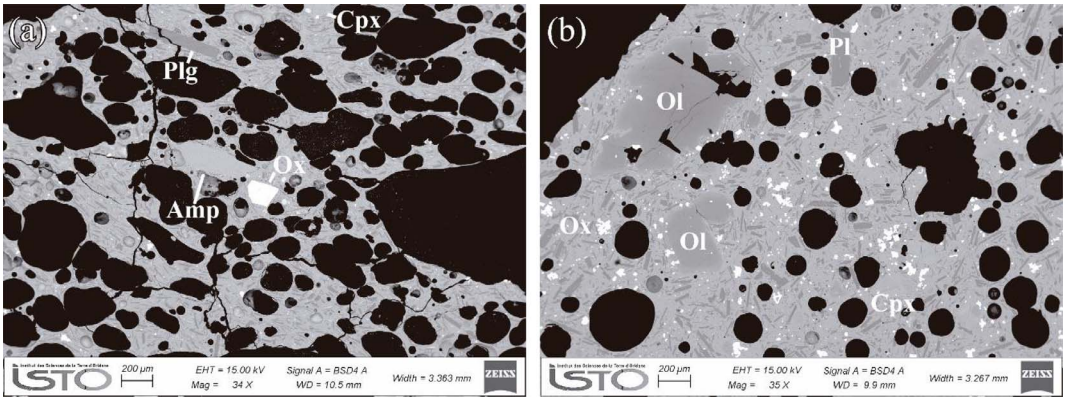

Supplementary Figure S1. Back-scattered electron images of the scoriae samples, showing (a) a general view of Garachico phonotephrite with clinopyroxene (Cpx), amphibole (Amp), plagioclase (Pl) and Fe–Ti magnetite (Ox) microphenocrysts. (b) A general view of Fasnia basanite with olivine (Ol) and clinopyroxene (Cpx) phenocrysts, plagioclase (Pl) and Fe–Ti magnetite (Ox) microphenocrysts.

with <5 wt.% of clinopyroxene, Ca-rich amphibole (kaersutite), Fe–Ti magnetite and plagioclase phenocrysts. The same phases plus Fe–Ti oxides and apatite are present as microphenocrysts (<0.15 mm) in a fine-grained glassy and vesiculated groundmass (Figure S1a). In comparison, the phenocrysts of Fasnia basanite are dominated by olivine, clinopyroxene and Fe–Ti magnetite [13 wt.%; Albert et al., 2015]. These phases, along with plagioclase, are also present as microphenocrysts in the glassy vesiculated groundmass of the scoriae (Figure S1b).

1.2. *Capsule preparation*

H_2O-saturated and CO_2-saturated charges were prepared separately using 2–2.5 cm long, 2.5 mm inner diameter and 0.2 mm wall thickness Au80–Pd20 capsules, which minimize iron loss during experiments under reduced conditions [Di Carlo et al., 2006]. Each capsule was prepared as follows: one end of the capsule was initially arc-welded and different amounts of the gas-source materials (H_2O or CO_2 see below) were first added into the capsules. For the set of H_2O solubility experiments, 3.5–8 μL of deionized water was added via a microsyringe, whereas for CO_2 solubility runs, silver oxalate ($Ag_2C_2O_4$) was used (3–9 mg): upon heating, this compound decomposes into metallic silver and pure CO_2 gas phase. After volatiles, glass chips <2 mm were loaded into the capsules in amounts (typically 60–80 mg) ensuring that fluid-saturated conditions were always achieved [e.g., Andújar and Scaillet, 2012b; Scaillet et al., 1995] (Table 2).

All capsules were weighed before and after adding each component and finally sealed by electric arc welding of the top end. After this step, if no significant loss occurred (difference <0.0004 g), they were left in an oven for several hours (~24 h) at 120 °C to ensure homogeneous fluid distribution and then weighed again. After the experiments, capsules were re-weighed to guarantee that no volatile loss had occurred and pierced for opening with cutting pliers. For H_2O experiments, the spur and/or the presence of small water bubbles hissing out from the capsules when opening confirmed that water-saturated conditions were attained.

1.3. *Experimental equipment and procedures*

A total set of 18 solubility experiments were conducted at the ISTO laboratory (Orléans, France) in internally heated pressure vessels (IHPV) operating vertically, using pure argon or a Ar–H2 gas mixture at room temperature as the pressure medium to achieve the desired fO_2 (see below).

Experiments were carried out at 1200 °C and pressures from 50 to 400 MPa (Table 2). The run duration was between 4 and 6 h, long enough to attain melt-fluid phase equilibrium under these conditions and to minimize iron-loss towards the capsule. Previous experimental studies on water and carbon diffusivities [e.g., Behrens and Zhang, 2001; Behrens et al.,

2004; Zhang et al., 1991], and redox reaction kinetics in silicate melts [Berndt et al., 2002; Gaillard et al., 2002; 2003a, 2003b] have shown that few hours (1–1.5 h) are sufficient to achieve the equilibrium between the melt and the fluid phase at these P–T conditions, especially in mafic to intermediate compositions [Behrens et al., 2009; Botcharnikov et al., 2005, 2006; Dixon et al., 1995; Lesne et al., 2011a, 2011b].

A typical run consisted of two capsules (one loaded with H_2O and the other with CO_2), wrapped in Pt cages and suspended by a Pt or Rh quench wire to the rapid-quench device. Heating was applied by a double-winding molybdenum furnace, which ensures a 3 cm long near-isothermal zone [±2–3 °C·cm^{-1}; Andújar et al., 2013] where the capsules are placed. The temperature was measured using two S-type thermocouples (accuracy of ± 5 °C) located on both the upper and lower parts of the T-homogeneous zone, allowing precise control of thermal gradients. The total pressure was recorded continuously by a transducer calibrated against a Heise Bourdon gauge with an uncertainty of ± 2 MPa [e.g., Di Carlo et al., 2006; Pichavant et al., 2009]. Experiments were ended using a rapid-quench technique with which the sample holder falls into the bottom part of the vessel and experiences isobaric quench at cooling rates >100 °C/s [Di Carlo et al., 2006]. All the experiments reported here showed a fast transient increase in total pressure of 10–40 bars upon the falling of the capsules, indicating that the drop quench was successful in each case.

It should be noted that in high pressure and H_2O-rich charges, quench crystals of 1–2 µm were observed (see Table 2). Similarly, under oxidising conditions (NNO + 3.2, see below), some basanitic and, to a lesser extent, phonotephritic, experimental glasses contained scarce amounts of Fe–Ti oxides (<7 wt.% as estimated from least-square mass-balance calculations; Table 2), which did not prevent, however, the acquisition of FTIR, EPMA and NanoSIMS data. Only charge F4b with $X_{H_2O} = 1$ and performed at 400 MPa (Table 2) contains slightly higher amounts of randomly distributed needle-shaped quench crystal aggregates that prevented the FTIR analysis from being performed. Consequently, for this charge, the glass water content was measured by the elemental analyzer and used, along with FTIR results, to complete the basanitic H_2O solubility dataset. Scarce microbubbles (<5–10 µm) to larger bubbles (0.3–0.5 mm) are located at the melt/capsule interface, mainly in CO_2 experiments, confirming that fluid saturation at given P and T was attained.

1.4. *Redox conditions of the experiments*

The effect of fO_2 on H_2O and CO_2 solubilities was explored by imposing two different oxygen fugacities in our experiments. The first set was pressurized with pure Ar, which corresponds to a $fO_2 \sim$ NNO + 3.2 (±0.1 log unit), where NNO is the nickel-nickel oxide buffer at the relevant P–T [Huebner and Sato, 1970]. The low amounts of quench phases are inconsequential to the interpretation of solubility trends. In all cases, the fO_2 of H_2O-bearing capsules is controlled by the fugacities of H_2 and H_2O through the reaction $H_2 + (1/2)O_2 \leftrightarrow H_2O$. Hence, to compute fO_2 in oxidizing experiments, we used the prevailing intrinsic fH_2 in the vessel (known from previous experiments performed in the same IHPV apparatus under similar P–T–fH_2 conditions [run 22 and run 23, Pichavant et al., 2009], the dissociation constant of water [from Robie et al., 1979], and the fugacity of pure water at the experimental P–T conditions [Burnham et al., 1969]. For CO_2-bearing charges, the fO_2 was determined considering the calculated fH_2O from the amount of dissolved water measured in each experimental product at any given P–T conditions (see below). A second set of experiments was performed under moderately reduced fO_2 conditions, which were obtained by pressurizing the vessel with an argon-hydrogen gas mixture equivalent to 1.5 bar H_2 of the total gas volume. For these runs, the prevailing fH_2 was independently determined using Ni–Pd–O solid sensors via two additional experiments run at 200 and 400 MPa at 1200 °C with the same H_2/Ar proportion but of longer duration (22–24 h). Sensors consisted of two pellets of Ni–Pd metal mixtures (each one with different Ni/Pd ratios) plus ZrO_2 as isolating material, placed in Au80–Pd20 capsules in the presence of excess H_2O following the procedure of Taylor et al. [1992]. The composition of the NiPd alloy was determined by electron microprobe analysis after the experiment, allowing fO_2 calculation of the sensor system from Pownceby and O'Neill's [1994] equation. Afterward, once the prevailing fO_2 is known, the fH_2 and the fO_2 of each charge was calculated as stated above. For the moderately reduced experiments, the oxygen fugacity was calculated to be ~NNO + 1.4

(±0.2 log unit). All experiments are reported in Tables 2 and 3.

Since the oxygen fugacity in capsules in H_2O-bearing systems is related to the fugacity of H_2 and H_2O through the water equilibrium reaction ($H_2 + (1/2)O_2 \leftrightarrow H_2O$), a decrease in fH_2O (or aH_2O) at constant fH_2 (the one prevailing in the vessel) is accompanied by a decrease in fO_2 [e.g., Scaillet et al., 1995; Webster et al., 1987]. It should be noted that, even if the CO_2 experiments were performed under nominally dry conditions (no H_2O added), they are not strictly water-free, as evidenced by the low amounts of water analysed in our experimental glasses (see below). Therefore, the fO_2 of CO_2-bearing charges was calculated using the fH_2O retrieved from our empirical equation relating fH_2O and melt water content, and the prevailing fH_2, as determined above. The calculated oxygen fugacity of CO_2-bearing experiments decreases by 1 to 3 log units relative to H_2O saturated conditions, depending on melt water content, as observed in other experimental studies [e.g., Behrens et al., 2009; Botcharnikov et al., 2005; Lesne et al., 2011a, 2011b; Webster et al., 1987; Table 2].

1.5. *Analytical methods*

1.5.1. *Major element compositions*

Starting materials and run products were mounted in epoxy resin, polished and analysed with a Cameca SX-Five electron microprobe at ISTO-BRGM (Orléans, France) (Table 1 and S1). Analytical conditions were: 15 kV accelerating voltage, beam current of 6 nA, counting times of 10 s and a defocused 20 µm beam diameter to minimize alkali migration [i.e., Andújar and Scaillet, 2012b; Morgan and London, 2005]. Sodium and potassium were analysed first to limit any loss and a Phi-Rho-Z correction procedure was applied. Major elements calibration has been performed using standards of (1) silicate minerals: albite (Na, Si), orthoclase (K), andradite (Ca) topaz (F); (2) phosphates: apatite (P), vanadinite (Cl); sulphates: baryte (S); and (3) oxides: chromite (Cr), corundum (Al), magnesium oxide (Mg), nickel oxide (Ni), hematite (Fe) and pyrophanite (Mn, Ti). For the oxides, the relative analytical errors are 1% (SiO_2, Al_2O_3, CaO), 3% (FeO, MgO, TiO_2) and 5% (MnO, Na_2O, K_2O, P_2O_5) [Di Carlo et al., 2006].

Metallic sensor phases were analysed under an accelerating voltage of 15 kV and a sample current of 20 nA, using pyrite, nickel, palladium and platinum as standards.

1.5.2. *Density*

The density of quenched glasses was measured using Archimedes' method in a Mettler Toledo AG balance equipped with a density accessory kit. Archimedes' principle states that a body immersed partially or fully in fluid experiences a buoyant force acting upwards on it, so the magnitude of this force is equivalent to the weight of the fluid displaced by the body. Thus, samples were weighed in air and then in absolute ethanol at a known atmospheric temperature, using the following equation to calculate the density:

$$\rho = A/((A-B)*(\rho_0-\rho_L)+\rho_L) \qquad \text{(S.1)}$$

where A is the weight in air, B is the weight in ethanol, ρ_0 is the density of ethanol and ρ_L is the density of air. The measurements were repeated 10 to 12 times on samples weighing from 5 up to 58 mg. Density measurements vary from 2626 to 2787 g/l for the basanite and from 2523 to 2669 g/l for the phonotephrite (Table 2). Analytical errors remain below 2.5% for most experimental glasses, reaching values between 3.1 and 4.8% in cases where large glass fragments were not available (<10–15 mg).

1.5.3. *Fourier transform infrared spectroscopy*

H_2O and CO_2 contents in experimental glasses were measured by FTIR spectroscopy (Table 2) on doubly polished glass chips with different thicknesses, ranging from 15 to 200 µm. The thickness at each analysis point was measured at least three times with a LEITZ DMR optical microscope equipped with an automated X–Y stage, enabling measurements within 2 µm. FTIR spectra were collected in transmission using a Nicolet 6700 FTIR spectrometer attached to an IR microscope (Nicolet Continuµm) equipped with a MCT detector at the ISTO-CNRS laboratory. A Globar light source, a XT-KBr beamsplitter and a 32x infinity-corrected Schwarzschild objective matching to 32x condenser were used to record absorbances of the fundamental OH-stretching vibration (~3520 cm^{-1}) and the carbonate doublet (~1430 cm^{-1} and ~1520 cm^{-1}) in the mid-infrared (MIR) region, as well as combination bands of molecular water

Supplementary Table S1. Composition of experimental glasses

	SiO_2	TiO_2	Al_2O_3	FeO^a	MnO	MgO	CaO	Na_2O	K_2O	P_2O_5	Total
F05	44.37	3.50	14.94	12.39	0.16	7.92	10.62	3.83	1.54	0.72	100
	0.33	*0.23*	*0.20*	*0.21*	*0.13*	*0.09*	*0.11*	*0.07*	*0.11*	*0.19*	
F1a	45.96	3.50	15.43	10.71	0.20	7.84	10.57	3.50	1.42	0.86	100
	0.30	*0.14*	*0.08*	*0.21*	*0.07*	*0.12*	*0.04*	*0.08*	*0.07*	*0.15*	
F1c	44.27	3.55	15.03	12.35	0.24	7.95	10.52	3.84	1.60	0.64	100
	0.26	*0.19*	*0.13*	*0.26*	*0.10*	*0.07*	*0.11*	*0.09*	*0.09*	*0.13*	
F2a	45.50	3.56	15.41	10.67	0.16	7.75	10.68	3.74	1.64	0.90	100
	0.26	*0.10*	*0.15*	*0.22*	*0.07*	*0.08*	*0.13*	*0.07*	*0.07*	*0.11*	
F2b	44.74	3.49	14.98	11.86	0.25	7.99	10.55	3.79	1.59	0.75	100
	0.32	*0.13*	*0.14*	*0.27*	*0.08*	*0.10*	*0.13*	*0.15*	*0.10*	*0.13*	
F3a	47.91	3.14	16.03	7.93	0.13	7.70	10.88	3.71	1.73	0.83	100
	0.22	*0.16*	*0.18*	*0.22*	*0.06*	*0.06*	*0.08*	*0.11*	*0.07*	*0.13*	
F3b	44.67	3.49	15.04	12.13	0.14	7.83	11.25	3.34	1.31	0.79	100
	0.30	*0.11*	*0.22*	*0.39*	*0.07*	*0.15*	*0.25*	*0.18*	*0.20*	*0.12*	
F3c1	44.90	3.75	15.12	11.90	0.18	7.87	10.81	3.20	1.54	0.71	100
	0.21	*0.20*	*0.15*	*0.15*	*0.10*	*0.13*	*0.15*	*0.13*	*0.13*	*0.17*	
F4a	48.21	3.04	16.16	7.41	0.10	7.88	11.37	3.24	1.65	0.93	100
	0.29	*0.11*	*0.11*	*0.15*	*0.05*	*0.06*	*0.06*	*0.13*	*0.06*	*0.16*	
F4b	44.60	3.54	15.12	11.82	0.20	7.77	10.67	3.99	1.63	0.67	100
	0.28	*0.18*	*0.16*	*0.23*	*0.08*	*0.14*	*0.17*	*0.12*	*0.09*	*0.13*	
FC05	45.01	3.58	15.24	10.93	0.21	7.99	10.71	3.89	1.69	0.74	100
	0.31	*0.11*	*0.23*	*0.35*	*0.12*	*0.06*	*0.12*	*0.10*	*0.10*	*0.15*	
FC1b	45.18	3.62	15.37	10.51	0.21	8.10	10.72	3.96	1.58	0.77	100
	0.32	*0.18*	*0.14*	*0.36*	*0.09*	*0.08*	*0.13*	*0.07*	*0.09*	*0.17*	
FC2b	45.51	3.69	15.38	9.97	0.13	8.20	10.77	3.92	1.64	0.79	100
	0.33	*0.16*	*0.30*	*0.27*	*0.10*	*0.15*	*0.09*	*0.12*	*0.10*	*0.09*	
FC3b	45.21	3.55	15.39	10.50	0.21	8.12	10.77	4.00	1.61	0.65	100
	0.32	*0.18*	*0.14*	*0.36*	*0.09*	*0.08*	*0.13*	*0.07*	*0.09*	*0.17*	
FC4b	45.85	3.58	15.54	9.69	0.18	8.12	10.71	3.98	1.61	0.75	100
	0.33	*0.16*	*0.30*	*0.27*	*0.10*	*0.15*	*0.09*	*0.12*	*0.10*	*0.09*	
G05	48.46	2.93	17.82	9.47	0.20	4.03	8.60	5.18	2.19	1.11	100
	0.25	*0.22*	*0.20*	*0.26*	*0.08*	*0.08*	*0.07*	*0.10*	*0.11*	*0.15*	
G1a	48.74	2.98	18.07	8.80	0.24	3.98	8.65	5.14	2.22	1.20	100
	0.39	*0.22*	*0.24*	*0.27*	*0.10*	*0.07*	*0.17*	*0.16*	*0.14*	*0.19*	
G1c	49.11	3.00	17.98	9.31	0.17	4.01	8.59	4.48	2.27	1.07	100
	0.35	*0.13*	*0.16*	*0.21*	*0.06*	*0.09*	*0.09*	*0.29*	*0.08*	*0.13*	
G2a	48.88	3.05	18.00	8.89	0.19	4.00	8.62	5.02	2.23	1.11	100
	0.20	*0.20*	*0.20*	*0.20*	*0.05*	*0.08*	*0.11*	*0.24*	*0.12*	*0.20*	

(continued on next page)

Supplementary Table S1. (continued)

	SiO_2	TiO_2	Al_2O_3	FeO[a]	MnO	MgO	CaO	Na_2O	K_2O	P_2O_5	Total
G2b	48.16	3.11	17.61	9.41	0.20	4.05	8.62	5.31	2.15	1.38	100
	0.18	*0.16*	*0.23*	*0.20*	*0.07*	*0.06*	*0.08*	*0.09*	*0.10*	*0.13*	
G3a	50.48	2.74	18.49	6.65	0.14	3.93	8.81	5.27	2.38	1.13	100
	0.39	*0.09*	*0.16*	*0.19*	*0.08*	*0.08*	*0.11*	*0.12*	*0.13*	*0.13*	
G4a	48.60	2.98	18.09	8.86	0.25	3.99	8.66	5.18	2.24	1.16	100
	0.26	*0.22*	*0.23*	*0.34*	*0.09*	*0.07*	*0.16*	*0.18*	*0.13*	*0.17*	
G4b	48.58	3.02	17.76	9.54	0.24	4.02	8.40	5.19	2.22	1.02	100
	0.26	*0.16*	*0.18*	*0.31*	*0.07*	*0.07*	*0.12*	*0.08*	*0.17*	*0.14*	
GC05	50.07	3.22	18.00	7.08	0.18	4.02	8.66	5.33	2.17	1.27	100
	0.29	*0.16*	*0.18*	*0.12*	*0.09*	*0.05*	*0.09*	*0.09*	*0.08*	*0.18*	
GC1a	48.36	2.99	17.81	9.53	0.25	4.02	8.51	5.17	2.21	1.15	100
	0.25	*0.16*	*0.28*	*0.17*	*0.10*	*0.06*	*0.06*	*0.14*	*0.08*	*0.17*	
GC2a	48.89	2.87	17.76	9.17	0.28	3.89	8.43	5.37	2.26	1.09	100
	0.26	*0.18*	*0.13*	*0.20*	*0.07*	*0.06*	*0.10*	*0.09*	*0.09*	*0.15*	
GC2b	48.90	3.14	17.85	8.16	0.19	4.07	8.62	5.52	2.25	1.29	100
	0.25	*0.12*	*0.18*	*0.12*	*0.10*	*0.05*	*0.11*	*0.09*	*0.09*	*0.14*	
GC3a	48.42	3.29	17.86	9.24	0.23	4.00	8.49	5.05	2.19	1.24	100
	0.34	*0.20*	*0.25*	*0.17*	*0.10*	*0.05*	*0.15*	*0.10*	*0.08*	*0.15*	
GC3b	50.03	2.94	18.20	7.22	0.16	4.06	8.69	5.46	2.29	0.94	100
	0.30	*0.18*	*0.17*	*0.26*	*0.10*	*0.08*	*0.14*	*0.12*	*0.11*	*0.26*	
GC4a	49.14	2.94	17.72	8.19	0.16	4.18	8.62	5.43	2.35	1.27	100
	0.37	*0.16*	*0.13*	*0.27*	*0.12*	*0.06*	*0.17*	*0.13*	*0.16*	*0.12*	
GC4b	49.94	3.03	18.09	7.12	0.18	4.04	8.73	5.60	2.25	1.02	100
	0.30	*0.18*	*0.17*	*0.26*	*0.10*	*0.08*	*0.14*	*0.12*	*0.11*	*0.26*	

Compositions normalized to 100% anhydrous melt.
Oxide concentrations were measured by EPMA at ISTO-CNRS.
[a] Total iron expressed as FeO.

(5200 cm^{-1}) and hydroxyl groups (4500 cm^{-1}) in the near-infrared (NIR) region (Table S3). For each analysis, 128 scans were collected in the range of 6000 to 655 cm^{-1} with an aperture of 50 × 50 µm and a spectral resolution of 4 cm^{-1}, collecting a background on CaF_2 (for H_2O) and NaCl (for CO_2) windows before each sample. Typically, three to seven spots were acquired in different parts of the glass chips to ensure the homogeneous distribution of the volatile phases over the samples and the results were then averaged.

The concentration of H_2O and CO_2 were determined using the Lambert-Beer law:

$$Ci = (M_i * A_j)/(\rho * d * \varepsilon_j) * 100 \qquad \text{(S.2)}$$

where C_i is the concentration of species i (in wt.%), M_i is the molecular weight of the species i, A_j is the absorbance (peak height of band j), ρ is the density of the run product (in g/L, see above), d is the thickness of the glass chip at each analysed point (in cm) and ε_j is the absorption coefficient of band j (in L/mol·cm).

For NIR and MIR water spectra, two tangents [TT baseline, Lesne et al., 2011a, 2011b; Ohlhorst et al., 2001; Schanofski et al., 2019] were applied to the base of the 4500 cm^{-1}, 5200 cm^{-1} and 3520 cm^{-1} bands to measure the peak heights (see Figure S2a, b). In the case of carbonate doublet, before the TT baseline

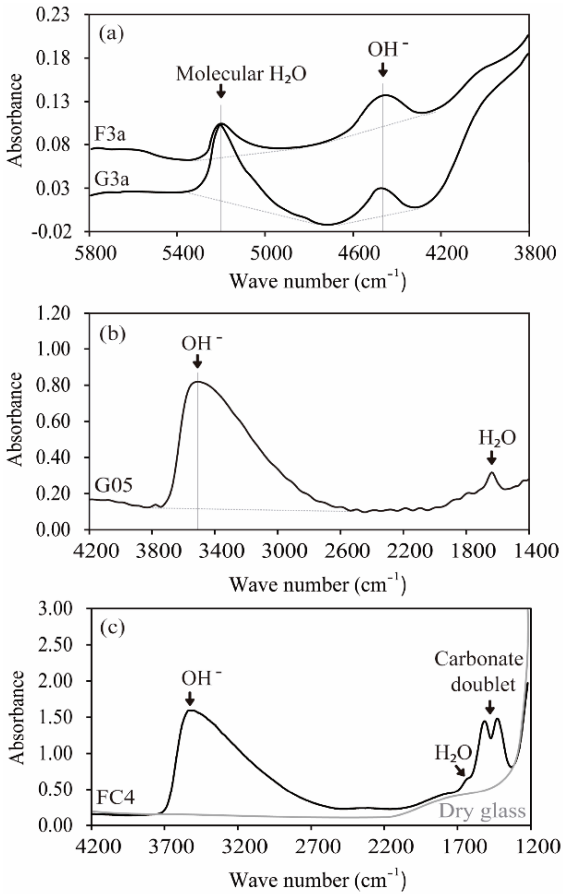

Supplementary Figure S2. Near-IR and Mid-IR representative spectra of different basanitic and phonotephritic experimental glasses. Bold lines represent measured spectra and grey lines the fitted baselines. (a) Molecular water band at 5200 cm^{-1} and the hydroxyl band at 4500 cm^{-1} of the F3a (6.14 wt.% H_2O) and G3a (6.32 wt.% H_2O) samples. (b) The absorbance of the fundamental OH- stretching vibration at about 3520 cm^{-1} of the G05 glass (2.35 wt.% H_2O). (c) The spectrum of the corresponding starting dry glass (thick grey line), scaled to the same thickness, was used for subtracting from the sample spectrum (FC4, 5748 ppm CO_2) to measure the peak heights of the carbonate peaks at 1430 cm^{-1} and 1520 cm^{-1}.

correction, a subtraction from volatile-free glasses with the same composition and normalized to the same thicknesses was applied (Figure S2c).

The lack of bulk H_2O and CO_2 data prevented us from determining molar absorption coefficients for the compositions studied here. To contour this limitation, we used absorption coefficients derived from magma compositions that closely approach those studied here. For the Fasnia basanite, water contents were quantified using the following absorption coefficients 0.56 ± 0.04 $L{\cdot}mol^{-1}{\cdot}cm^{-1}$ and 0.58 ± 0.02 $L{\cdot}mol^{-1}{\cdot}cm^{-1}$ for ε_{5200} and ε_{4500}, respectively [Cocheo, 1993], and 59.2 ± 4 $L{\cdot}mol^{-1}{\cdot}cm^{-1}$ for ε_{3520} [Shishkina et al., 2014]; whereas for the Garachico phonotephrite 1.02 ± 0.03 $L{\cdot}mol^{-1}{\cdot}cm^{-1}$, 0.62 ± 0.06 $L{\cdot}mol^{-1}{\cdot}cm^{-1}$ and 63.9 ± 5.4 $L{\cdot}mol^{-1}$ cm^{-1} we used for ε_{5200}, ε_{4500} and ε_{3520}, respectively [Behrens et al., 2009].

Despite that no water was added to the CO_2-solubility charges, our FTIR spectra show that all run products contained small amounts of dissolved water (≤2 wt%; Table 2; Figure S2c). For this reason,

the carbonate band at 1520 cm^{-1} was slight to moderately affected by the H_2O bending at 1630 cm^{-1} and could not be used for CO_2 quantification purposes [e.g., Behrens et al., 2009; Botcharnikov et al., 2006; Shishkina et al., 2014]. Therefore, we used the 1430 cm^{-1} peak to calculate the dissolved CO_2 in all experimental glasses considering the absorption coefficients of 283 ± 8 $L{\cdot}mol^{-1}{\cdot}cm^{-1}$ for Fasnia basanite [Dixon and Pan, 1995] and 264 ± 15 $L{\cdot}mol^{-1}{\cdot}cm^{-1}$ for Garachico phonotephrite [Vetere et al., 2014].

Considering the strong dependence of the absorption coefficient with composition, the major source of error associated with our FTIR H_2O–CO_2 quantifications comes from the use of coefficient values that have not been specifically calibrated for our magmas [e.g., Dixon and Pan, 1995; Dixon et al., 1995; Mandeville et al., 2002]. Notwithstanding, the errors associated with the volatile-content quantification were calculated by propagating errors associated to absorbance, density, absorption coefficient, and thickness. Calculated errors are about 5–15%, i.e., similar to those of previous studies [Behrens et al., 2009; Iacono-Marziano et al., 2012; Lesne et al., 2011a, 2011b; Shishkina et al., 2014].

As in previous studies [e.g., Allison et al., 2019; von Aulock et al., 2014], we observed a good correlation between peaks height and water concentration in the glass, since the difference between contents determined using the ~3500 cm^{-1} peak and those from near-IR data is usually <0.15 wt.% (Table 2). However, for data discussion and further comparison, we preferred to use here the results from the combination of the molecular water (5200 cm^{-1}) and hydroxyl groups (4500 cm^{-1}) bands, as their propagated errors are less than 10% compared to those associated with the fundamental band (15%). Such a difference (5%) arises from the necessity of using relatively thin glass wafers (i.e., 15–40 μm thickness) to ensure (1) a good proportionality between peak heights and water contents and (2) avoiding peak-detector saturation. However, despite this technical advantage, the accuracy of ±2 μm in the thickness measurement propagates into higher relative errors when using relatively thin wafers for determining melt water concentrations.

1.5.4. *Nanoscale secondary ion mass spectrometry*

Experimental glasses were also analysed using the Cameca NanoSIMS 50 installed at the Muséum National d'Histoire Naturelle in Paris with the aim of verifying the suitability of the selected absorption coefficients to retrieve H_2O and CO_2 contents from our experimental glasses. We could apply this procedure since the NanoSIMS independently measures the OH/Si and C/Si ratios of the sample so that if the entered values of H_2O and CO_2 do not match with the measured ratios, a calibration regression line cannot be established. For this reason, we used our H_2O and CO_2 experimental glasses as NanoSIMS secondary standards obtaining, in this case, a good regression of the data (as evidenced by the $R^2 = 0.99$; Figure S3), which validates our previous choice concerning the absorption coefficients for both compositions to determine H_2O and CO_2 contents using FTIR.

NanoSIMS analyses were performed using a 19 pA Cs^+ primary beam rastered over 3 × 3 μm^2 surface area. However, to avoid surface contamination, only ions from the inner 1.5 × 1.5 μm^2 were collected using the "beam blanking" mode. Secondary ions of $^{12}C^-$, $^{16}OH^-$ and $^{28}Si^-$were recovered in multicollection mode. Mass resolving power was set at a minimum of 5600, a value which is sufficient to resolve interferences on $^{16}OH^-$. A single analysis comprises a stack of 100 cycles, each lasting for 1.024 s. An electron flooding gun was used for charge compensation. Prior to each analysis, a 235 pA Cs^+ primary beam was used for presputtering over 5 × 5 μm^2 surface area for 2 min to remove surface contamination and reach a steady-state sputtering [Thomen et al., 2014]. The vacuum in the analysis chamber remained below 2×10^{-10} Torr during measurements. Once optimal analytical conditions were achieved, the H_2O and CO_2 contents of the experimental glasses were determined through the measurement of $^{16}OH^-/^{28}Si^-$ and $^{12}C^-/^{28}Si^-$ ratios, respectively. Concentrations and uncertainties were determined using the R program following the procedure described in Bartoli et al. [2014] and Thomen et al. [2014].

1.5.5. *Elemental analyzer*

As we pointed out in previous sections, despite the systematic use of the rapid-quench device in our experiments, one charge (F4b, Table 2) presented quench mineral phases in proportions and with distributions that did not allow direct measurements with FTIR or NanoSIMS. Therefore, we determined the bulk H_2O-content of 9 run products with a

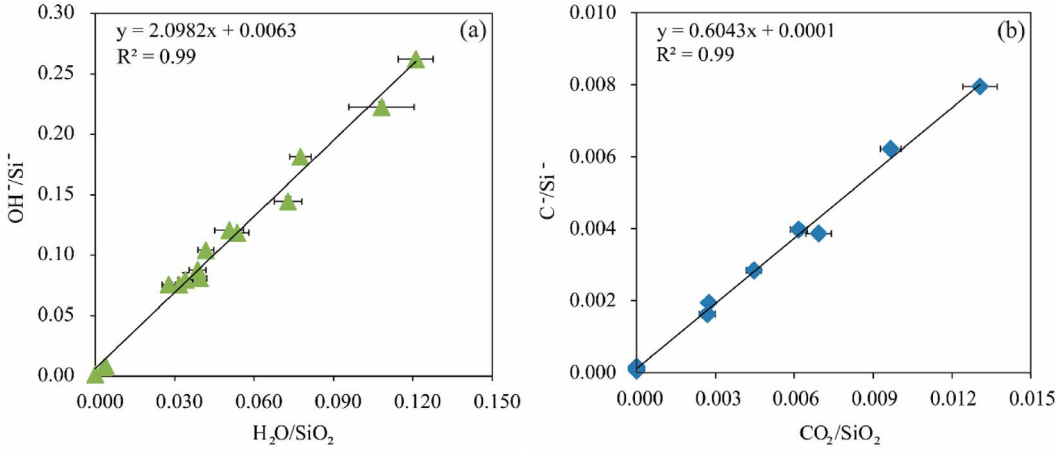

Supplementary Figure S3. NanoSIMS calibration curves. (a) Correlation between the measured OH^-/Si^- ratio by the NanoSIMS vs. the H_2O/SiO_2 ratio measured by FTIR and EPMA, respectively, on H_2O-saturated experiments (green triangles). (b) NanoSIMS C^-/Si^- ratio vs. CO_2/SiO_2 on CO_2-saturated experimental glasses (blue diamonds).

Thermo Scientific™ FLASH™ 2000 CHNS/O located at ISTO (see Table 2), measuring H concentration in glasses and hence, H_2O as follows. 10–15 mg of glassy material was first weighed, loaded to a tin capsule, and introduced into the combustion reactor via the Thermo Scientific MAS 200R Autosampler. The glass is then dropped into an oxidation/reduction reactor kept at a temperature of 900–1000 °C for its full combustion. The produced gases are carried out by a helium flow towards a layer filled with copper, then swept through a chromatographic column to separate them, and finally, detected by a thermal conductivity detector (TCD).

Typically, each analysis started with a calibration step consisting of a series of blank measurements followed by standard inner measurements containing already known H_2O contents (from 2.74 to 12 wt.%). Each experimental glass set was then loaded and analysed to retrieve the hydrogen concentration which, via the previous calibration data, was finally used to calculate H_2O concentrations in glasses.

Supplementary Table S2. Comparison between H_2O and CO_2 results from this study and other author's models.

		wt% H_2O (this study)		wt% H_2O (from other H_2O models)				Equilibrium pressure model (Iacono-Marziano et al., 2012)[a]
Sample	P (MPa)	wt% H_2O	wt% H_2O Error	wt% H_2O Iacono-Marziano et al. (2012)	wt% H_2O Error Iacono-Marziano et al. (2012)	wt% H_2O Lesne et al. (2011a)	wt% H_2O Shishkina et al. (2014)	P (MPa)
F1a	100	3.37	0.26	3.71	0.44	3.33	3.55	73
F2a	210	4.82	0.35	5.88	0.75	5.21	5.83	120
F3a	292	6.14	0.32	7.24	0.97	6.78	6.94	162
F4a	411	7.35	0.48	8.97	1.28	8.38	9.10	201
F05	52	2.29	0.19	2.53	0.28	2.13	2.43	40
F1c	108	3.25	0.17	3.90	0.46	3.28	3.81	69
F2b	210	5.03	0.27	5.88	0.75	5.12	5.83	127
F3c2	319	6.17	0.38	7.66	1.04	6.77	7.76	164
F4b	397	7.26	0.35	8.78	1.25	8.24	8.67	198
G1a	100	3.36	0.24	2.68	0.29	3.42	3.83	126
G2a	210	5.12	0.30	4.20	0.49	5.45	6.33	226
G3a	292	6.32	0.34	5.14	0.62	7.13	7.48	293
G4a	411	7.38	0.35	6.34	0.81	8.89	9.95	350
G05	52	2.35	0.25	1.84	0.19	2.15	2.58	73
G1b	108	3.67	0.23	2.81	0.30	3.38	4.13	143
G2b	207	5.24	0.52	4.17	0.48	5.35	6.23	233
G4b	413	7.56	0.40	6.36	0.82	8.81	10.04	359

		CO_2 (ppm, this study)				CO_2 (ppm, from other CO_2 models)			H_2O-CO_2 model (Iacono-Marziano et al., 2012)				Equilibrium pressure model (Iacono-Marziano et al., 2012)[b]	
Sample	P (MPa)	CO_2 (ppm)	CO_2 error (ppm)	wt% H_2O	wt% H_2O error	CO_2 (ppm) Iacono-Marziano et al. (2012)	CO_2 error (ppm) Iacono-Marziano et al. (2012)	CO_2 ppm Shishkina et al. (2014)	CO_2 (ppm)	CO_2 Error (ppm)	wt% H_2O	wt% H_2O Error	P (MPa)	P Error (MPa)
FC05	60	484	35	1.19	0.10	437	150	511	461	174	1.25	0.14	62	17
FC1c	113	1205	55	1.49	0.03	910	314	1053	1000	398	1.59	0.19	129	35
FC2b	210	2713	138	1.70	0.14	1973	688	2141	2221	923	1.80	0.22	244	69
FC3b	294	4208	169	1.72	0.11	3211	1128	3153	3469	1443	1.76	0.22	339	93
FC4b	397	5748	287	1.84	0.13	4645	1640	4454	5234	2205	1.79	0.22	423	111
GC1a	10	620	49	0.30	0.03	1142	370	552	1173	382	0.20	0.02	57	17
GC2a	19	1291	146	0.19	0.02	2478	812	1151	2401	788	0.12	0.01	112	33
GC4a	40	3046	249	0.24	0.03	5833	1938	2639	5852	1948	0.14	0.01	237	63
GC05	6	278	24	1.17	0.10	548	176	301	548	184	0.85	0.08	47	10
GC2b	21	1419	93	1.27	0.11	2478	812	1242	2533	866	0.90	0.09	138	35
GC3b	294	2166	134	1.35	0.12	4032	1331	1856	3938	1360	0.93	0.09	191	49
GC4b	413	3356	235	1.54	0.13	5833	1938	2748	6199	2176	1.01	0.11	269	68

[a] Equilibrium pressure model (Iacono-Marziano et al., 2012) computed using H_2O-saturated experimental data from this study

[b] Equilibrium pressure model (Iacono-Marziano et al., 2012) computed using CO2-saturated experimental data from this study
See section 4.2 and 4.4 for explanation

Supplementary Table S3. FTIR absorbance and thickness measurements from experimental glasses.

Sample	A_{3520}	sd A_{3520}	A_{4500}	sd A_{4500}	A_{5200}	sd A_{5200}	A_{1430}	sd A_{1430}	Thickness (cm)	Density (g/l)	sd density
F05_analysis01	0.8255	0.0014							0.0040	2748	28
F05_analysis02	0.8719	0.0015							0.0042	2748	28
F05_analysis03	0.8690	0.0011							0.0042	2748	28
F05_analysis04	0.8491	0.0013							0.0041	2748	28
F1a_analysis01	0.4700	0.0005							0.0017	2669	83
F1a_analysis02	0.4817	0.0009							0.0017	2669	83
F1a_analysis03	0.4480	0.0015							0.0016	2669	83
F1a_analysis04	0.4670	0.0019							0.0016	2669	83
F1c_analysis01	1.2867	0.0018							0.0045	2750	23
F1c_analysis02	1.2839	0.0031							0.0045	2750	23
F1c_analysis03	1.3442	0.0007							0.0045	2750	23
F1c_analysis04	1.3533	0.0023							0.0046	2750	23
F1a_2_analysis01			0.0089	0.0005	0.0101	0.0010			0.0066	2669	83
F1a_2_analysis02			0.0081	0.0002	0.0085	0.0008			0.0060	2669	83
F1a_2_analysis03			0.0094	0.0005	0.0079	0.0009			0.0060	2669	83
F1c_2_analysis01			0.0209	0.0006	0.0201	0.0021			0.0141	2750	22
F1c_2_analysis02			0.0204	0.0008	0.0182	0.0005			0.0141	2750	22
F1c_2_analysis03			0.0198	0.0005	0.0201	0.0006			0.0140	2750	22
F1c_2_analysis04			0.0193	0.0001	0.0199	0.0011			0.0139	2750	22
F2a_analysis01	0.8031	0.0007							0.0020	2626	65
F2a_analysis02	0.7521	0.0023							0.0018	2626	65
F2a_analysis03	0.7020	0.0010							0.0017	2626	65
F2a_analysis04	0.9974	0.0009							0.0024	2626	65
F2a_analysis05	0.7991	0.0023							0.0020	2626	65
F2a_analysis06	0.6790	0.0006							0.0017	2626	65
F2b_analysis01	0.9208	0.0031							0.0021	2720	28
F2b_analysis02	0.9802	0.0013							0.0022	2720	28
F2b_analysis03	0.8586	0.0009							0.0019	2720	28
F2b_analysis04	0.9979	0.0009							0.0022	2720	28
F2b_analysis05	0.7585	0.0005							0.0017	2720	28
F2b_analysis06	1.1293	0.0027							0.0025	2720	28
F2b_analysis07	0.9195	0.0010							0.0021	2720	28
F2a_2_analysis01			0.0108	0.0008	0.0112	0.0006			0.0056	2626	65
F2a_2_analysis02			0.0107	0.0011	0.0119	0.0006			0.0055	2626	65
F2a_2_analysis03			0.0099	0.0006	0.0117	0.0010			0.0056	2626	65
F2b_2_analysis01			0.0227	0.0004	0.0319	0.0004			0.0126	2720	27
F2b_2_analysis02			0.0237	0.0004	0.0314	0.0005			0.0128	2720	27
F2b_2_analysis03			0.0153	0.0004	0.0306	0.0022			0.0125	2720	27
F2b_2_analysis04			0.0232	0.0015	0.0347	0.0011			0.0133	2720	27
F3a_analysis01	1.4714	0.0027							0.0027	2785	87
F3a_analysis02	1.5263	0.0117							0.0027	2785	87
F3a_analysis03	1.4602	0.0049							0.0026	2785	87
F3a_analysis04	1.4784	0.0034							0.0027	2785	87
F3c2_analysis01	1.0156	0.0002							0.0019	2727	32
F3c2_analysis02	1.0166	0.0020							0.0019	2727	32
F3c2_analysis03	1.0107	0.0013							0.0019	2727	32
F3a_2_analysis01			0.0212	0.0001	0.0425	0.0008			0.0131	2785	87
F3a_2_analysis02			0.0256	0.0003	0.0419	0.0001			0.0130	2785	87
F3a_2_analysis03			0.0263	0.0000	0.0411	0.0008			0.0127	2785	87
F3a_2_analysis04			0.0298	0.0004	0.0388	0.0005			0.0130	2785	87
F3b_2_analysis01			0.0088	0.0002	0.0481	0.0004			0.0094	2657	27
F3b_2_analysis02			0.0123	0.0006	0.0518	0.0003			0.0100	2657	27
F3b_2_analysis03			0.0084	0.0008	0.0459	0.0003			0.0091	2657	27
F3b_2b_analysis01			0.0118	0.0001	0.0479	0.0002			0.0113	2727	31
F3b_2b_analysis02			0.0113	0.0008	0.0488	0.0002			0.0113	2727	31

F3b_2b_analysis03			0.0108	0.0001	0.0478	0.0008	0.0113	2727	31
F4a_analysis04	1.2698	0.0027					0.0020	2690	61
F4a_analysis05	1.1611	0.0018					0.0018	2690	61
F4a_analysis06	1.1497	0.0023					0.0018	2690	61
F4a_analysis07	1.4527	0.0033					0.0023	2690	61
F4a_analysis08	1.4426	0.0017					0.0023	2690	61
F4a_2_analysis01			0.0145	0.0004	0.0627	0.0007	0.0123	2690	61
F4a_2_analysis02			0.0124	0.0002	0.0583	0.0007	0.0117	2690	61
F4a_2_analysis03			0.0127	0.0005	0.0595	0.0009	0.0116	2690	61
G05_analysis01	0.7060	0.0011					0.0032	2661	30
G05_analysis02	0.6970	0.0016					0.0031	2661	30
G05_analysis03	0.6694	0.0018					0.0030	2661	30
G05_analysis04	0.7011	0.0023					0.0032	2661	30
G1a_analysis02	0.8598	0.0019					0.0028	2523	78
G1a_analysis03	0.8529	0.0028					0.0028	2523	78
G1a_analysis04	0.8373	0.0038					0.0027	2523	78
G1b_analysis01	0.6511	0.0005					0.0020	2543	16
G1b_analysis02	0.7353	0.0025					0.0022	2543	16
G1b_analysis03	0.6793	0.0011					0.0020	2543	16
G1b_analysis04	0.7364	0.0017					0.0022	2543	16
G1a_2_analysis01			0.0196	0.0001	0.0304	0.0021	0.0129	2523	78
G1a_2_analysis02			0.0187	0.0009	0.0303	0.0016	0.0129	2523	78
G1a_2_analysis03			0.0190	0.0009	0.0301	0.0026	0.0128	2523	78
G1b_2_analysis01			0.0219	0.0004	0.0292	0.0010	0.0122	2543	16
G1b_2_analysis02			0.0209	0.0006	0.0291	0.0013	0.0122	2543	16
G1b_2_analysis03			0.0201	0.0014	0.0303	0.0018	0.0120	2543	16
G2a_analysis01	1.1803	0.0053					0.0027	2533	81
G2a_analysis02	1.2177	0.0052					0.0028	2533	81
G2a_analysis03	1.2277	0.0040					0.0028	2533	81
G2b_analysis01	1.3795	0.0011					0.0028	2632	16
G2b_analysis02	1.3786	0.0108					0.0028	2632	16
G2b_analysis03	1.3574	0.0107					0.0027	2632	16
G2b_analysis04	1.3595	0.0065					0.0026	2632	16
G2b_analysis05	1.2836	0.0062					0.0026	2632	16
G2a_2_analysis01			0.0276	0.0005	0.0436	0.0005	0.0125	2533	81
G2a_2_analysis02			0.0280	0.0001	0.0459	0.0012	0.0126	2533	81
G2a_2_analysis03			0.0297	0.0003	0.0439	0.0018	0.0129	2533	81
G2a_2_analysis04			0.0265	0.0011	0.0460	0.0010	0.0120	2533	81
G2b_2_analysis01			0.0201	0.0013	0.0560	0.0116	0.0115	2632	16
G2b_2_analysis02			0.0230	0.0013	0.0532	0.0044	0.0118	2632	16
G2b_2_analysis03			0.0233	0.0016	0.0551	0.0070	0.0119	2632	16
G3a_analysis01	1.2815	0.0043					0.0022	2642	89
G3a_analysis02	1.2930	0.0027					0.0022	2642	89
G3a_analysis03	1.0622	0.0012					0.0018	2642	89
G3a_analysis04	1.2036	0.0064					0.0021	2642	89
G3a_2_analysis01			0.0316	0.0012	0.0796	0.0021	0.0139	2642	89
G3a_2_analysis02			0.0338	0.0005	0.0789	0.0013	0.0139	2642	89
G3a_2_analysis03			0.0317	0.0005	0.0776	0.0010	0.0142	2642	89
G3a_2_analysis04			0.0335	0.0010	0.0812	0.0014	0.0140	2642	89
G3a_2_analysis06			0.0317	0.0009	0.0773	0.0022	0.0140	2642	89
G4a_analysis01	1.1481	0.0054					0.0017	2567	61
G4a_analysis03	1.1559	0.0049					0.0018	2567	61
G4a_analysis04	1.1704	0.0042					0.0018	2567	61
G4a_analysis05	1.1409	0.0046					0.0017	2567	61
G4b_analysis01	1.1964	0.0064					0.0018	2551	27
G4b_analysis02	1.2403	0.0079					0.0023	2551	27
G4b_analysis03	1.6140	0.0231					0.0025	2551	27
G4b_analysis04	1.6076	0.0176					0.0025	2551	27
G4a_2_analysis01			0.0288	0.0003	0.0780	0.0002	0.0120	2567	61
G4a_2_analysis02			0.0282	0.0015	0.0814	0.0003	0.0120	2567	61
G4a_2_analysis03			0.0300	0.0008	0.0825	0.0003	0.0119	2567	61
G4b_2_analysis01			0.0126	0.0006	0.0914	0.0038	0.0102	2551	27

G4b_2_analysis02			0.0121	0.0004	0.0922	0.0048			0.0102	2551	27
G4b_2_analysis03			0.0123	0.0008	0.0889	0.0038			0.0102	2551	27
FC05_analysis01							0.1667	0.0130	0.0174	2746	34
FC05_analysis02							0.1475	0.0071	0.0174	2746	34
FC05_analysis03							0.1448	0.0158	0.0174	2746	34
FC05_analysis04							0.1433	0.0001	0.0183	2746	34
FC1c_analysis02							0.2768	0.0122	0.0124	2787	33
FC1c_analysis03							0.2729	0.0064	0.0125	2787	33
FC1c_analysis04							0.2608	0.0043	0.0126	2787	33
FC2b_analysis01							0.2473	0.0013	0.0051	2748	23
FC2b_analysis02							0.2454	0.0033	0.0050	2748	23
FC2b_analysis03							0.2189	0.0007	0.0047	2748	23
FC2b_analysis05							0.2368	0.0024	0.0049	2748	23
FC3b_analysis01							0.8635	0.0179	0.0115	2771	31
FC3b_analysis02							0.8629	0.0098	0.0115	2771	31
FC3b_analysis03							0.8634	0.0210	0.0116	2771	31
FC4b_analysis02							0.5174	0.0051	0.0050	2779	19
FC4b_analysis03							0.5143	0.0034	0.0050	2779	19
FC4b_analysis04							0.5124	0.0003	0.0050	2779	19
FC05_water__analysis01	0.5145	0.0008							0.0046	2746	33
FC05_water__analysis02	0.5388	0.0019							0.0049	2746	33
FC05_water__analysis04	0.5292	0.0007							0.0052	2746	33
F05_water__analysis01	0.6963	0.0016							0.0048	2787	32
FC1c_water__analysis02	0.6645	0.0004							0.0047	2787	32
FC1c_water__analysis03	0.6346	0.0002							0.0047	2787	32
FC1c_water__analysis04	0.6359	0.0005							0.0050	2787	32
FC1c_water__analysis05	0.6548	0.0008							0.0047	2787	32
FC1c_water__analysis06	0.6365	0.0005							0.0050	2787	32
FC2b_water__analysis01	0.7922	0.0021							0.0051	2748	22
FC2b_water__analysis02	0.8079	0.0017							0.0050	2748	22
FC2b_water__analysis03	0.7738	0.0013							0.0047	2748	22
FC2b_water__analysis05	0.7820	0.0024							0.0049	2748	22
FC3b_water__analysis01	0.7797	0.0009							0.0057	2771	30
FC3b_water__analysis02	0.7898	0.0042							0.0059	2771	30
FC3b_water__analysis03	0.7810	0.0017							0.0059	2771	30
FC4b_water__analysis01	1.4703	0.0081							0.0086	2779	18
FC4b_water__analysis02	1.4295	0.0095							0.0086	2779	18
FC4b_water__analysis03	1.4242	0.0119							0.0087	2779	18
FC4b_water__analysis04	1.4821	0.0043							0.0088	2779	18
FC4b_water__analysis05	1.4709	0.0077							0.0084	2779	18
FC4b_water__analysis06	1.4103	0.0079							0.0087	2779	18
GC05_analysis01							0.0609	0.0022	0.0147	2651	30
GC05_analysis02							0.0724	0.0031	0.0146	2651	30
GC05_analysis03							0.0663	0.0050	0.0144	2651	30
GC05_analysis04							0.0565	0.0054	0.0143	2651	30
GC1a_analysis01							0.2032	0.0124	0.0200	2669	49
GC1a_analysis02							0.2009	0.0066	0.0198	2669	49
GC1a_analysis03							0.1879	0.0105	0.0199	2669	49
GC2a_analysis02							0.2989	0.0252	0.0126	2654	99
GC2a_analysis03							0.2905	0.0279	0.0166	2654	99
GC2b_analysis01							0.1884	0.0032	0.0084	2638	33
GC2b_analysis02							0.1827	0.0062	0.0081	2638	33
GC2b_analysis03							0.1886	0.0026	0.0082	2638	33
GC2b_analysis04							0.1863	0.0019	0.0084	2638	33
GC2b_analysis05							0.1936	0.0022	0.0087	2638	33
GC3b_analysis01							0.3341	0.0030	0.0101	2548	34
GC3b_analysis02							0.3536	0.0025	0.0105	2548	34
GC3b_analysis03							0.3474	0.0041	0.0106	2548	34
GC3b_analysis04							0.3654	0.0000	0.0106	2548	34
GC3b_analysis05							0.3463	0.0026	0.0112	2548	34
GC3b_analysis06							0.3682	0.0028	0.0112	2548	34
GC3b_analysis07							0.3146	0.0017	0.0099	2548	34

GC3b_analysis08			0.3376	0.0016	0.0099	2548	34
GC3b_analysis09			0.2972	0.0000	0.0090	2548	34
GC3b_analysis10			0.3138	0.0021	0.0092	2548	34
GC4a_analysis01			0.3525	0.0072	0.0073	2586	124
GC4a_analysis02			0.3390	0.0072	0.0073	2586	124
GC4a_analysis03			0.3542	0.0069	0.0073	2586	124
GC4a_analysis04			0.3352	0.0065	0.0073	2586	124
GC4a_analysis05			0.3600	0.0063	0.0074	2586	124
GC4a_analysis06			0.3475	0.0064	0.0074	2586	124
GC4b_analysis01			0.6470	0.0190	0.0126	2555	27
GC4b_analysis02			0.6825	0.0261	0.0128	2555	27
GC4b_analysis03			0.6355	0.0260	0.0128	2555	27
GC05_water_analysis01	1.6072	0.0124			0.0147	2651	30
GC05_water_analysis02	1.5834	0.0034			0.0146	2651	30
GC05_water_analysis03	1.6064	0.0034			0.0144	2651	30
GC05_water_analysis04	1.5803	0.0126			0.0143	2651	30
GC1a_water_analysis01	0.3827	0.0018			0.0131	2669	49
GC1a_water_analysis02	0.3895	0.0003			0.0131	2669	49
GC1a_water_analysis03	0.3521	0.0016			0.0131	2669	49
GC1a_water_analysis04	0.3567	0.0007			0.0131	2669	49
GC2a_water_analysis01	0.2190	0.0000			0.0129	2654	99
GC2a_water_analysis02	0.2432	0.0000			0.0126	2654	99
GC2a_water_analysis03	0.2671	0.0000			0.0166	2654	99
GC2b_water_analysis01	0.9810	0.0039			0.0084	2638	33
GC2b_water_analysis02	0.9645	0.0036			0.0081	2638	33
GC2b_water_analysis03	0.9795	0.0030			0.0080	2638	33
GC2b_water_analysis04	0.9448	0.0020			0.0077	2638	33
GC2b_water_analysis05	0.9856	0.0048			0.0082	2638	33
GC2b_water_analysis06	0.9758	0.0041			0.0084	2638	33
GC2b_water_analysis07	1.0051	0.0034			0.0087	2638	33
GC3b_water_analysis01	1.2566	0.0017			0.0101	2548	34
GC3b_water_analysis02	1.3051	0.0020			0.0105	2548	34
GC3b_water_analysis03	1.2711	0.0061			0.0106	2548	34
GC3b_water_analysis04	1.3421	0.0095			0.0112	2548	34
GC3b_water_analysis05	1.1847	0.0054			0.0099	2548	34
GC3b_water_analysis06	1.1080	0.0062			0.0090	2548	34
GC3b_water_analysis07	1.1421	0.0043			0.0092	2548	34
GC4a_water_analysis01	0.1764	0.0011			0.0073	2586	124
GC4a_water_analysis02	0.1671	0.0012			0.0073	2586	124
GC4a_water_analysis03	0.1585	0.0018			0.0074	2586	124
GC4b_water_analysis01	1.5300	0.0120			0.0109	2555	27
GC4b_water_analysis03	1.5658	0.0081			0.0110	2555	27
GC4b_water_analysis04	1.5999	0.0128			0.0116	2555	27
GC4b_water_analysis05	1.6094	0.0289			0.0116	2555	27
GC4b_water_analysis06	1.5716	0.0152			0.0113	2555	27
GC4b_water_analysis07	1.5562	0.0040			0.0113	2555	27

Absorbances of the fundamental OH-stretching vibration (~3520 cm^{-1}) and the carbonate doublet (~1430 cm^{-1} and ~1520cm^{-1}) in the mid-infrared (MIR) region, and the combination bands of molecular water (5200cm-1) and hydroxyl groups (4500cm^{-1}) in the near-infrared region (NIR). Errors represent the standard deviations of the measured absorbances.

Thickness uncertainty correspond to the microscope instrumental error (0.0002 cm)

Density measured using Archimedes' method. Standard deviations correspond to 10-12 density measurements of each glass fragment

References

Ablay, G. J., Carroll, M. R., Palmer, M. R., Marti, J., and Sparks, R. S. J. (1998). Basanite–phonolite lineages of the Teide–Pico Viejo volcanic complex, Tenerife, Canary Island. *J. Petrol.*, 39(5), 905–936.

Albert, H., Costa, F., and Martí, J. (2015). Timing of magmatic processes and unrest associated with mafic historical monogenetic eruptions in Tenerife island. *J. Petrol.*, 56, 1945–1966.

Allison, C. M., Roggensack, K., and Clarke, A. B. (2019). H_2O–CO_2 solubility in alkali-rich mafic magmas: new experiments at mid-crustal pressures. *Contrib. Mineral. Petrol.*, 174, article no. 58.

Andújar, J., Costa, F., and Scaillet, B. (2013). Storage conditions and eruptive dynamics of central versus flank eruptions in volcanic islands: the case of Tenerife (Canary Islands, Spain). *J. Volcanol. Geotherm. Res.*, 260, 62–79.

Andújar, J. and Scaillet, B. (2012b). Relationships between pre-eruptive conditions and eruptive styles of phonolite–trachyte magmas. *Lithos*, 152, 122–131.

Bartoli, O., Cesare, B., Remusat, L., Acosta-Vigil, A., and Poli, S. (2014). The H_2O content of granite embryos. *Earth Planet. Sci. Lett.*, 395, 281–290.

Behrens, H., Misiti, V., Freda, C., Vetere, F., Botcharnikov, R. E., and Scarlato, P. (2009). Solubility of H_2O and CO_2 in ultrapotassic melts at 1200 and 1250 C and pressure from 50 to 500 MPa. *Amer. Miner.*, 94, 105–120.

Behrens, H., Ohlhorst, S., Holtz, F., and Champenois, M. (2004). CO_2solubility in dacitic melts equilibrated with H_2O-CO_2 fluids: Implications for modeling the solubility of CO_2 in silicic melts. *Geochim. Cosmochim. Acta*, 68, 4687–4703.

Behrens, H. and Zhang, Y. (2001). Ar diffusion in hydrous silicic melts: implications for volatile diffusion mechanisms and fractionation. *Earth Planet. Sci. Lett.*, 192, 363–376.

Berndt, J., Liebske, C., Holtz, F., Freise, M., Nowak, M., Ziegenbein, D., Hurkuck, W., and Koepke, J. (2002). A combined rapid-quench and H_2-membrane setup for internally heated pressure vessels: Description and application for water solubility in basaltic melts. *Amer. Miner.*, 87, 1717–1726.

Botcharnikov, R., Freise, M., Holtz, F., and Behrens, H. (2005). Solubility of C–O–H mixtures in natural melts: new experimental data and application range of recent models. *Ann. Geophys.*, 48, 633–646.

Botcharnikov, R. E., Behrens, H., and Holtz, F. (2006). Solubility and speciation of C–O–H fluids in andesitic melt at T = 1100–1300 °C and P = 200 and 500 MPa. *Chem. Geol.*, 229, 125–143.

Burnham, C. W., Holloway, J. R., and Davis, N. F. (1969). *Thermodynamic properties of water to 1,000 °C and 10,000 bars*, volume 132. Geological Society of America.

Carracedo, J. C. and Perez-Torrado, F. J. (2013). Geological and geodynamic context of the Teide volcanic complex. In Carracedo, J. C. and Troll, V. R., editors, *Teide Volcano: Geology and Eruptions of a Highly Differentiated Oceanic Stratovolcano, Active Volcanoes of the World*, pages 23–36. Springer, Berlin, Heidelberg.

Cocheo, P. A. (1993). The solubility of water in basanitic melts at low pressures. Master's thesis. Arizona State University.

Di Carlo, I., Pichavant, M., Rotolo, S. G., and Scaillet, B. (2006). Experimental crystallization of a high-K arc basalt: the Golden Pumice, Stromboli volcano (Italy). *J. Petrol.*, 47, 1317–1343.

Dixon, J. E. and Pan, V. (1995). Determination of the molar absorptivity of dissolved carbonate in basanitic glass. *Am. Miner.*, 80, 1339–1342.

Dixon, J. E., Stolper, E. M., and Holloway, J. R. (1995). An Experimental study of water and carbon dioxide solubilities in Mid-Ocean Ridge Basaltic liquids. Part I: Calibration and solubility models. *J. Petrol.*, 36, 1607–1631.

Gaillard, F., Pichavant, M., and Scaillet, B. (2003a). Experimental determination of activities of FeO and Fe_2O_3 components in hydrous silicic melts under oxidizing conditions. *Geochim. Cosmochim. Acta*, 67, 4389–4409.

Gaillard, F., Scaillet, B., and Pichavant, M. (2002). Kinetics of iron oxidation-reduction in hydrous silicic melts. *Amer. Miner.*, 87, 829–837.

Gaillard, F., Schmidt, B., Mackwell, S., and McCammon, C. (2003b). Rate of hydrogen–iron redox exchange in silicate melts and glasses. *Geochim. Cosmochim. Acta*, 67, 2427–2441.

Huebner, J. S. and Sato, M. (1970). The oxygen fugacity-temperature relationships of manganese oxide and nickel oxide buffers. *Amer. Miner.*, 55, 934–952.

Iacono-Marziano, G., Morizet, Y., Le Trong, E., and Gaillard, F. (2012). New experimental data and

semi-empirical parameterization of H_2O–CO_2 solubility in mafic melts. *Geochim. Cosmochim. Acta*, 97, 1–23.

Le Bas, M. J., Maitre, R. W. L., Streckeisen, A., and Zanettin, B. (1986). IUGS Subcommission on the Systematics of Igneous Rocks. A chemical classification of volcanic rocks based on the total alkali-silica diagram. *J. Petrol.*, 27, 745–750.

Lesne, P., Scaillet, B., Pichavant, M., and Beny, J.-M. (2011b). The carbon dioxide solubility in alkali basalts: an experimental study. *Contrib. Mineral. Petrol.*, 162, 153–168.

Lesne, P., Scaillet, B., Pichavant, M., Iacono-Marziano, G., and Beny, J.-M. (2011a). The H_2O solubility of alkali basaltic melts: an experimental study. *Contrib. Mineral. Petrol.*, 162, 133–151.

Mandeville, C. W., Webster, J. D., Rutherford, M. J., Taylor, B. E., Timbal, A., and Faure, K. (2002). Determination of molar absorptivities for infrared absorption bands of H_2O in andesitic glasses. *Amer. Miner.*, 87, 813–821.

Morgan, G. B. and London, D. (2005). Effect of current density on the electron microprobe analysis of alkali aluminosilicate glasses. *Amer. Miner.*, 90, 1131–1138.

Ohlhorst, S., Behrens, H., and Holtz, F. (2001). Compositional dependence of molar absorptivities of near-infrared OH- and H_2O bands in rhyolitic to basaltic glasses. *Chem. Geol.*, 174, 5–20. 6th International Silicate Melt Workshop.

Pichavant, M., Di Carlo, I., Le Gac, Y., Rotolo, S. G., and Scaillet, B. (2009). Experimental constraints on the deep magma feeding system at Stromboli volcano, Italy. *J. Petrol.*, 50, 601–624.

Pownceby, M. I. and O'Neill, H. S. C. (1994). Thermodynamic data from redox reactions at high temperatures. IV. Calibration of the Re–ReO_2 oxygen buffer from EMF and NiO+Ni−Pd redox sensor measurements. *Contrib. Mineral. Petrol.*, 118, 130–137.

Robie, R. A., Hemingway, B. S., and Fisher, J. R. (1979). *Thermodynamic Properties of Minerals and Related Substances at 298.15 K and 1 Bar (10^5 Pascals) Pressure and at Higher Temperatures*, volume 1452 of *U. S. Geol. Surv. Bull.* https://doi.org/10.3133/b1452.

Scaillet, B., Pichavant, M., and Roux, J. (1995). Experimental crystallization of leucogranite magmas. *J. Petrol.*, 36, 663–705.

Schanofski, M., Fanara, S., and Schmidt, B. C. (2019). CO_2–H_2O solubility in K-rich phonolitic and leucititic melts. *Contrib. Mineral. Petrol.*, 174, article no. 52.

Shishkina, T. A., Botcharnikov, R. E., Holtz, F., Almeev, R. R., Jazwa, A. M., and Jakubiak, A. A. (2014). Compositional and pressure effects on the solubility of H_2O and CO_2 in mafic melts. *Chem. Geol.*, 388, 112–129.

Solana, M. C. (2012). Development of unconfined historic lava flow fields in Tenerife: implications for the mitigation of risk from a future eruption. *Bull. Volcanol.*, 74, 2397–2413.

Taylor, J. R., Wall, V. J., and Pownceby, M. I. (1992). The calibration and application of accurate redox sensors. *Amer. Miner.*, 77, 284–295.

Thomen, A., Robert, F., and Remusat, L. (2014). Determination of the nitrogen abundance in organic materials by NanoSIMS quantitative imaging. *J. Anal. At. Spectrom.*, 29, 512–519.

Vetere, F., Holtz, F., Behrens, H., Botcharnikov, R. E., and Fanara, S. (2014). The effect of alkalis and polymerization on the solubility of H_2O and CO_2 in alkali-rich silicate melts. *Contrib. Mineral. Petrol.*, 167, article no. 1014.

von Aulock, F. W., Kennedy, B. M., Schipper, C. I., Castro, J. M., Martin, D. E., Oze, C., Watkins, J. M., Wallace, P. J., Puskar, L., Bégué, F., Nichols, A. R. L., and Tuffen, H. (2014). Advances in Fourier transform infrared spectroscopy of natural glasses: From sample preparation to data analysis. *Lithos*, 206–207, 52–64.

Webster, J. D., Holloway, J. R., and Hervig, R. L. (1987). Phase equilibria of a Be, U and F-enriched vitrophyre from Spor Mountain, Utah. *Geochim. Cosmochim. Acta*, 51, 389–402.

Zhang, Y., Stolper, E. M., and Wasserburg, G. J. (1991). Diffusion of water in rhyolitic glasses. *Geochim. Cosmochim. Acta*, 55, 441–456.